

Journal of MARINE RESEARCH

Volume 61, Number 5

Wave-induced boundary mixing in a partially mixed estuary

by Daniel Bourgault^{1,2} and Daniel E. Kelley¹

ABSTRACT

We present observations that reveal the existence of horizontally propagating, tidally-driven, high-frequency internal wave (IW) packets in a channel of the partially mixed St. Lawrence Estuary. The packets propagate transversely to the channel axis and collide with the shoaling lateral boundaries. The structure and energy of IWs are diagnosed with a two-dimensional, nonlinear nonhydrostatic model, and the results are compared with weakly nonlinear Korteweg-de-Vries (KdV) theory. The behavior of IWs running into the shoaling lateral boundary is examined in terms of published laboratory and numerical experiments. Our analysis indicates that IWs break on the slope, during which 6% of their energy is converted into potential energy through vertical mixing. The corresponding buoyancy flux, when averaged over the surf zone and the time of the mixing event, is more than an order of magnitude larger than values predicted by a published non-IW-resolving three-dimensional (3D) baroclinic circulation model of the region. Even averaging across the full domain and tidal period yields mixing rates that are a significant proportion of those in the 3D circulation model. These indirect inferences suggest that wave-induced boundary mixing may be of general significance in partially mixed estuaries.

1. Introduction

Contradictions between direct measurements of mixing in the ocean interior and inferences from one-dimensional pycnocline models have strengthened Munk's (1966) "boundary mixing" hypothesis, in which intense mixing near ocean boundaries is combined with lateral spreading of mixed water into the ocean interior (Armi, 1978; Munk and Wunsch, 1998). It has been proposed that breaking internal waves are largely responsible for this boundary mixing (see reviews by Garrett *et al.* (1993) and Munk and Wunsch (1998), and a more recent treatment of the propagation issue by Alford (2003)). Internal

1. Department of Oceanography, Dalhousie University, Halifax, NS, Canada B3H 4J1.

2. Present address: Department of Physics and Physical Oceanography, Memorial University of Newfoundland, St. John's, Newfoundland, Canada A1B 3X7. *email: danielb@physics.mun.ca*

wave breaking on shoaling boundaries has also been suggested to contribute significantly to vertical diffusion in lakes (Imberger and Hamblin, 1982; Goudsmit *et al.*, 1997; Imberger and Ivey, 1991; MacIntyre *et al.*, 1999) as well as in fjords (Stigebrandt, 1976, 1979; Perkin and Lewis, 1978; Farmer and Freeland, 1983; Stigebrandt and Aure, 1989). However, there have been few investigations of the role of wave-induced boundary mixing on estuaries. Given the importance of mixing to estuarine circulation and ecosystem dynamics (Legendre, 1981), and given that internal waves are commonly observed in such regions, further study is warranted.

Since bottom boundary-induced turbulence is greatly suppressed by salt stratification in highly and partially mixed estuaries (Jay and Smith, 1990a,b; Geyer, 1993), other mechanisms must be invoked to explain turbulent mixing in such systems (see e.g. Dyer (1988) for a review on estuarine classification). In highly stratified estuaries, shear instability driven by the combination of mean vertical shear and internal-wave shear is thought to be the main mixing agency (Geyer and Smith, 1987; Kay and Jay, 2003a, b). In partially mixed estuaries two views are opposed, or maybe complementary, as to what drives turbulent mixing. On the one hand, Jay and Smith (1990a) (p. 712) advanced that “. . . shear instabilities cannot be the primary vertical exchange mechanism in . . . partially mixed estuaries because there is no strong, tidal frequency internal circulation to generate strong shear in the interior, where the mixing of salt and fresh water occurs” and hypothesized that mixing mainly arises from internal wave breaking. On the other hand, the observations of Peters and Bokhorst (2000) suggest that mixing is triggered by instabilities that are driven by a vertical shear set up throughout the water column by the bottom shear stress. A similar finding was made by Stacey *et al.* (1999) who described estuarine mixing as a bottom mixed-layer deepening process induced by friction near the estuary bed, thus leaving internal waves to a secondary role in estuarine mixing. With this context, the present paper provides evidence of wave-induced mixing in a partially mixed estuary. Our focus is on horizontally propagating internal gravity waves (IW, henceforth) with frequency close to the buoyancy frequency. Our goal is to infer the mixing that results when IW encounter sloping boundaries.

The plan of the paper is as follows. First, the reader is introduced to the study area (Section 2) and to IW observations we have made there (Section 3). To aid in the analysis of these observations, we have set up a nonhydrostatic two-dimensional model; the details of the model, and the inferences it has helped us make about the propagation and the structure of the IW, are presented in Section 4. Combining the observations, the model simulations, and published laboratory experiments, we then infer the mixing rate induced by the collision of IWs with the lateral boundary (Section 5). A discussion follows of the mixing rates caused by other mixing agencies (Section 6), along with concluding remarks (Section 7).

2. Geographical context and oceanographic background

The St. Lawrence Estuary (SLE henceforth) is 500 km, widening from 2 km near the head to 50 km at the mouth (Fig. 1). A sudden change in the bottom topography (slope \sim

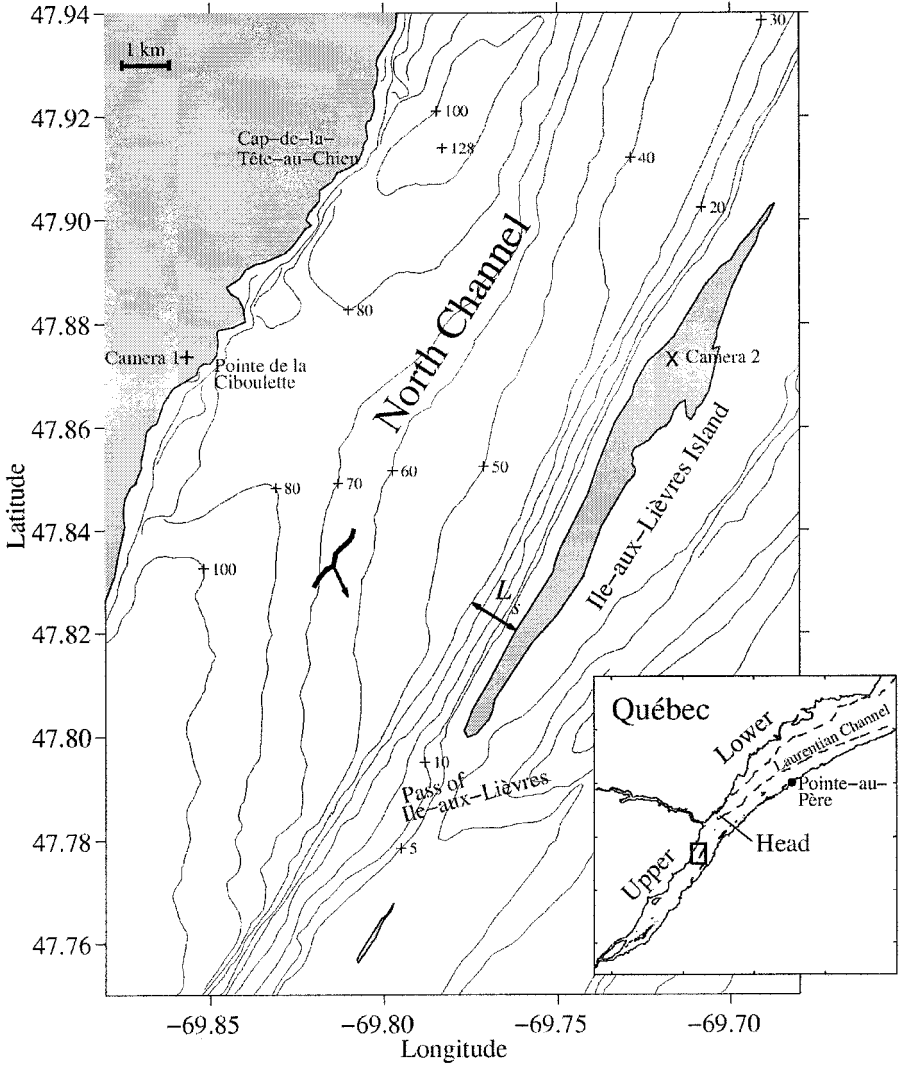


Figure 1. Study region in the St. Lawrence Estuary. The thick line in the middle of the North Channel indicates the ship track for the observations of Figure 2. The arrow next to the ship track indicates the direction of propagation of the wavetrain of Figure 2. Camera 1 (+ near Pointe de la Ciboulette) and Camera 2 (x on Ile-aux-Lièvres Island) indicate the locations of shore-based camera deployments. The double-arrowhead perpendicular to Ile-aux-Lièvres Island is a measure of the typical length of the slope L_s . The inset shows the whole St. Lawrence Estuary, divided into an upper and a lower section. The dashed line in the inset is the 200 m isobath.

1°) near the head of the deep (350 m) Laurentian Channel divides the estuary into upper and lower sections. The SLE receives freshwater mainly from the St. Lawrence River, at an annual mean discharge rate of $10^4 \text{ m}^3 \text{ s}^{-1}$ (Bourgault and Koutitonsky, 1999). Intense tidal currents (up to 3 m s^{-1}) produce well-mixed conditions near the head¹ of the estuary, but

farther seaward, as the estuary becomes wider (10–25 km) and deeper (50–150 m), the water column shows partially mixed conditions (see Dickie and Trites, 1983; El-Sabh, 1988; Koutitonsky and Bugden, 1991, for reviews of the oceanography of the SLE).

Reid (1977) showed that the dominant M_2 barotropic tide loses its energy mainly in the upper SLE. Using his estimates (from his Table 1) for the M_2 barotropic tidal energy fluxes through several lateral cross sections, we calculate the barotropic tidal loss to be $W_L \approx 0.06 \text{ W m}^{-2}$ and $W_U \approx 0.8 \text{ W m}^{-2}$ when averaged over the areas of the lower and upper estuary, respectively. Ultimately, this energy extracted from the barotropic tide is either dissipated into heat or used to increase the potential energy of the water column through vertical mixing. The intermediate steps in this energy pathway need to be clarified, including the fraction of W_U entering the internal tidal wave field (Forrester, 1974; Muir, 1979, 1981; Saucier and Chassé, 2000) and the IW fields. Our work addresses some of these issues.

Many types of observation reveal that IW are prominent in the upper SLE (DeGuise, 1977; Bourgault *et al.*, 2001) and near the boundary between the upper and the lower estuary (Ingram, 1978; Simard, 1985; Galbraith, 1992; Saucier and Chassé, 2000). Mertz and Gratton (1990) suggested that IW can trigger mixing in the SLE, but they also noted that sampling wave-induced mixing is a difficult task, owing to the complexity of the bottom topography and the short temporal scale (\sim min) and spatial scale (\sim 100 m) of IW. For this reason, most discussions of the role of IW in mixing SLE's waters has been somewhat qualitative. An exception is Galbraith's (1992) calculation of mixing rates associated with large-amplitude internal solitary waves observed near the head of the Laurentian Channel (inset in Fig. 1). Using a technique described by Galbraith and Kelley (1996) to infer mixing rates from density inversions, Galbraith estimated the associated turbulent buoyancy flux to be 20 times larger than that induced by the internal tidal shear. This made him suggest that IWs are a dominant source for turbulent mixing in the SLE, and form a motivation for our own field observations, described next.

3. Observations

We have observed IWs in a 15 km long stretch of the North Channel of the SLE (Fig. 1). The circulation in the North Channel is dominated by mixed semi-diurnal tidal currents of $1.5 \pm 0.75 \text{ m s}^{-1}$ amplitude (Government of Canada, 1997; Saucier and Chassé, 2000) that produce partially mixed conditions (El-Sabh, 1988).

a. Acoustic backscatter

Figure 2 shows an echogram depicting an internal wavetrain observed during early flood tide in the middle of the channel by Bourgault *et al.* (2001).³ This wavetrain is composed of

3. For ease of comparison with the Canadian Tide and Current Tables (Government of Canada, 2000) and the Atlas of Tidal Currents (Government of Canada, 1997), the time in the text and figures will be expressed either as Eastern Standard Time (EST = Greenwich Mean Time + 5 hours) or as the number of hours relative to the time of low-water (LW, henceforth) at the Pointe-au-Père tidal gauge.

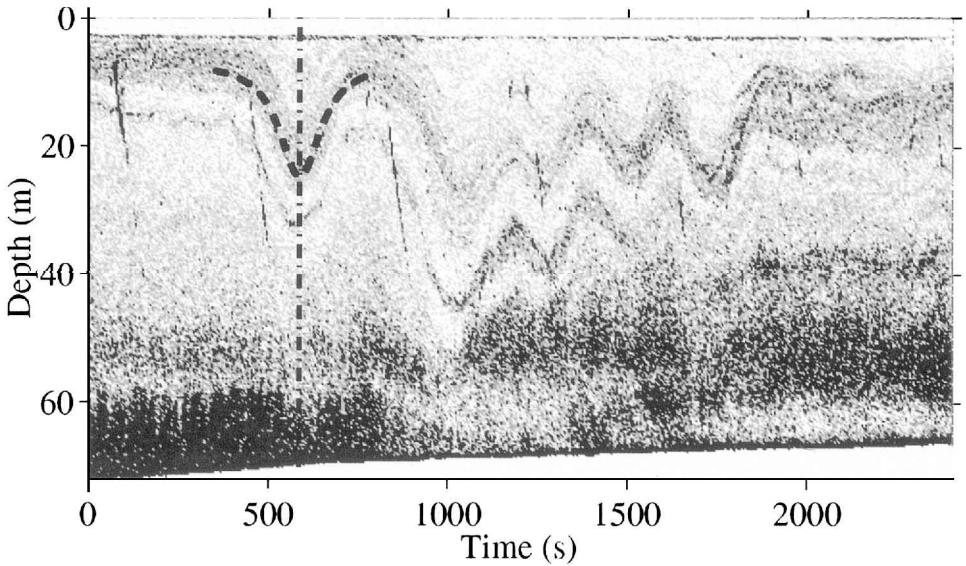


Figure 2. Echo-sounding image showing the large-amplitude internal wavetrain observed by Bourgault *et al.* (2001) on August 20, 1997 from a drifting ship (see Fig. 1 for ship track). This image was collected from LW + 2.40 to LW + 3.07. The oblique line fragments are reflections from the conductivity-temperature-depth probe (CTD). The dashed curve represents a best fit of the function defined by Eq. 8 to the digitized wave interface. The vertical dashed-dotted line represents the section where velocity data are presented in Figure 4.

5 waves of variable amplitude with the leading one exhibiting the shape of an internal solitary wave (ISW, henceforth) of depression (Osborne and Burch, 1980). This indication of nonlinear dynamics is consistent with the fact that the amplitude of the first wave, $a_0 = 16$ m, is almost twice the undisturbed surface layer thickness ($h_1 = 9$ m, Fig. 3). The trailing waves also have large amplitudes and might be ISWs or a trailing tail that generally follows ISWs (Osborne and Burch, 1980).

Figure 4 shows averaged profiles of the magnitude and direction of the baroclinic horizontal velocity (i.e., total minus depth-averaged) centered around the time of maximum wave displacement for the leading ISW (dashed-dotted line on Fig. 2). Since the flows in the upper (0–25 m) and lower (25–60 m) layers are 180° out of phase, we infer that the wave is of mode 1. The direction of ISW wave propagation is given by the direction of the wave-induced surface flow. We determined the latter by averaging the baroclinic velocity measurements over the top 25 m. The results indicate that the wavetrain propagates at 115° clockwise from north (vector on Fig. 1), thus heading toward Ile-aux-Lièvres Island and the shallow (<5 m) pass of Ile-aux-Lièvres Island, 4 km ahead.

b. Remote sensing

In the Summer of 2000 and 2002, remote sensing observations of the sea surface signature of IWs (e.g. Osborne and Burch, 1980) were acquired using shore-based still

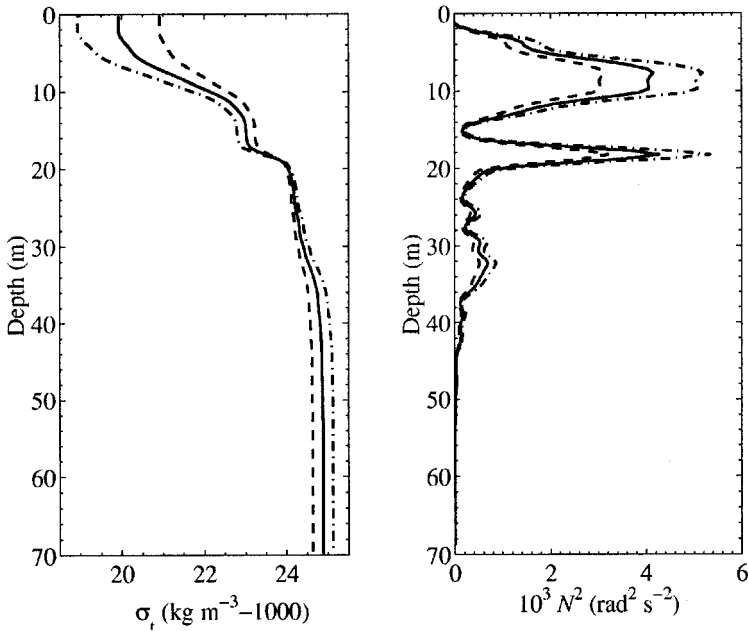


Figure 3. Profiles of density (left) and buoyancy frequency squared (right). The solid line is the observed profile prior to the passage of the wavetrain of Figure 2. The dashed and dashed-dotted lines are 25% increase/decrease in N^2 relative to the observed one. Those profiles are used for the numerical simulations (Section 4).

photography (“Camera 1” and “Camera 2” on Fig. 1). Observations were during a spring tide interval, and were centered around the early flood tide phase, on several days. This corresponds to the time when IWs were most expected to occur according to the observations of Bourgault *et al.* (2001). The time and details of each experiment are listed in Table 1.

Figure 5 shows the field of view of Camera 1. The dark bandlike structures seen between the island and the nearshore are taken to be surface manifestations of IW. We geometrically rectified the images for the pan, pitch and swing following Holland *et al.* (1997) and Pawlowicz (2003). Table 2 summarizes the resolution and error estimates of resultant images. Unable to devise a simple automatic identification of IW bands, we examined the images frame by frame, and digitized every recognizable long lasting band-like feature.

Figure 6 shows a 15-min interval sequence of bands typical of those observed from Camera 1. The prominent feature is the two distinct wavetrains appearing at time LW + 2.50. Wavetrain A is a series of 3 to 4 bands separated by a distance of 220 m to 300 m, and heading toward the coastline at a phase speed of $c_A = 0.7 \text{ m s}^{-1}$. Collision with the coastline occurs between LW + 3.25 and LW + 3.75. By LW + 4.00 no surface signature of wavetrain A is visible in the field of view. We found no evidence of reflection at the coastline, although some reflection is to be expected (e.g. Michallet and Ivey, 1999, Fig. 8).

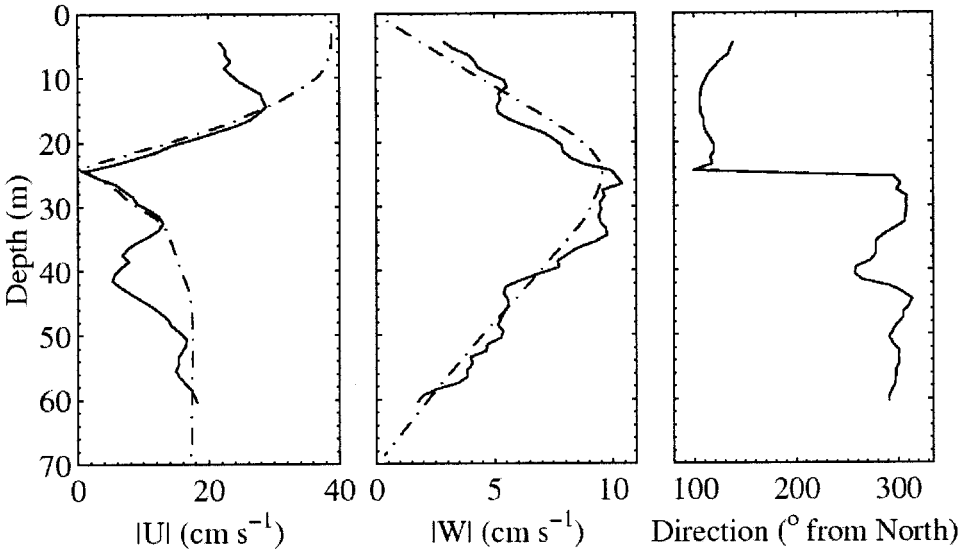


Figure 4. Four-minute averages, centered around the time of maximum interface displacement of the leading ISW of Figure 2, of the observed (solid line) profiles of the magnitude of the baroclinic horizontal velocity (left), magnitude of the vertical velocity (middle) and direction (right). For comparison, the dashed-dotted lines are 4-minute averages, centered around the time of maximum interface displacement, for the modeled ISW shown on the right panel of Figure 9.

It must be kept in mind, however, that absence of bandlike features in the images does not prove the absence of IWs.

Wavetrain B appears in the field of view as a series of 4 to 5 bands. Within the group, the distance between bands decreases from the leading one. The average distances between the first three sequential bands at LW + 3.50 are 400, 370 and 170 m. This is an indication that this group of waves consists of one or more ISWs with the fastest wave leading the group

Table 1. Details of remote sensing observations. The time is given in Eastern Standard Time (EST = Greenwich Mean Time + 5 hours). LW represents the time of low-water at the Pointe-au-Père tidal gauge (Government of Canada, 2000). PC is for Pointe-de-la-Ciboulette, AP is for airplane and IL is for Ile-aux-Lièvres Island. $\Delta\tau$ is the sampling time interval (min) between consecutive photographs.

Date	Position	Altitude (m)	Start	End	LW	$\Delta\tau$
2000/07/15	47°52.46'N 69°51.55'W (PC)	280	0800	1158	0800	2
2000/07/31	47°52.46'N 69°51.55'W (PC)	280	1039	1313	0825	2
2000/08/01	47°52.46'N 69°51.55'W (PC)	280	1010	1520	0910	2
2000/28/29	48°05.00'N 69°38.00'W (AP)	2500	1105	—	0805	—
2002/07/31	47°52.42'N 69°43.13'W (IL)	70	1220	1725	1240	5
2002/18/01	47°52.42'N 69°43.13'W (IL)	70	0700	1117	0555	5

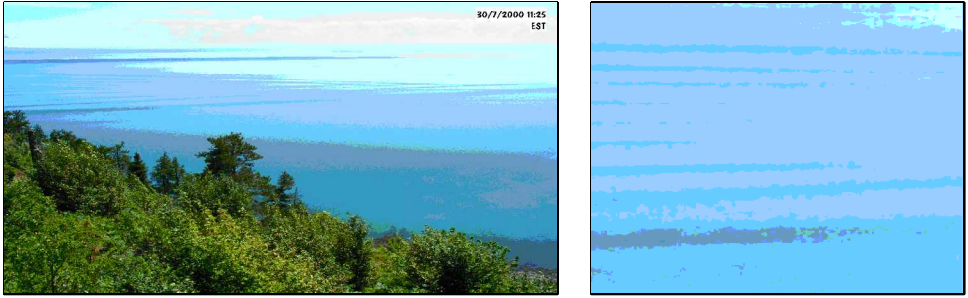


Figure 5. Field of view (left panel) of Camera 1, looking southeast, showing surface manifestations of IWs (details on the right panel). This image was taken on July 31, 2000 at LW + 3.00.

(Osborne and Burch, 1980). The direction of propagation is southeast and the phase speed is $c_B = 0.8 \text{ m s}^{-1}$. This wavetrain collides with an angle of approximately 45° with the southern end of Ile-aux-Lièvres Island from LW + 3.75 to LW + 4.25.

The bottom right panel of Figure 6 shows the wavetrains frontal positions at 15 min intervals. The distance between wave front positions is quite constant and, since the phase speed of an ISW is a function of its amplitude (e.g. Osborne and Burch, 1980), this suggests that the wavetrain energy, being proportional to the wave amplitude squared, does not significantly dissipate en route, so that most of the IW energy is carried all the way to the solid boundary.

Turning now to the north side of Ile-aux-Lièvres Island, Figure 7 shows the field of view of Camera 2. Here again, surface signatures of IW were clearly seen. Often more than a dozen bands, aligned approximately parallel to the flank of the island, could be observed in single snapshots. (The exact angle of incidence is difficult to determine since there were too few ground control points to permit geometric correction.) An almost continuous flux of shoreward propagating IWs were observed between LW + 2.00 to LW + 5.00 suggesting the collision with the island of more than one wavetrain per tidal cycle.

A larger view of the whole region is provided in Figure 8, which shows a geometrically rectified photograph of the North Channel taken from an aircraft at LW + 3.00. The image shows banded patterns similar to ones observed with the shore-based cameras (compare

Table 2. Resolution and uncertainty estimates on georectified images collected from Camera 1 in the Summer of 2000. Since the error increases with distances from the camera we give two estimates, one representative for the mid-channel and one for the far field.

Parameter	Far field (10 km offshore)	Mid-channel (5 km offshore)
Pixel resolution	150 m	35 m
Position uncertainty	$\pm 300 \text{ m}$	$\pm 70 \text{ m}$
Distance uncertainty	$\pm 80 \text{ m}$	$\pm 20 \text{ m}$
Phase speed uncertainty	$\pm 0.3 \text{ m s}^{-1}$	$\pm 0.08 \text{ m s}^{-1}$

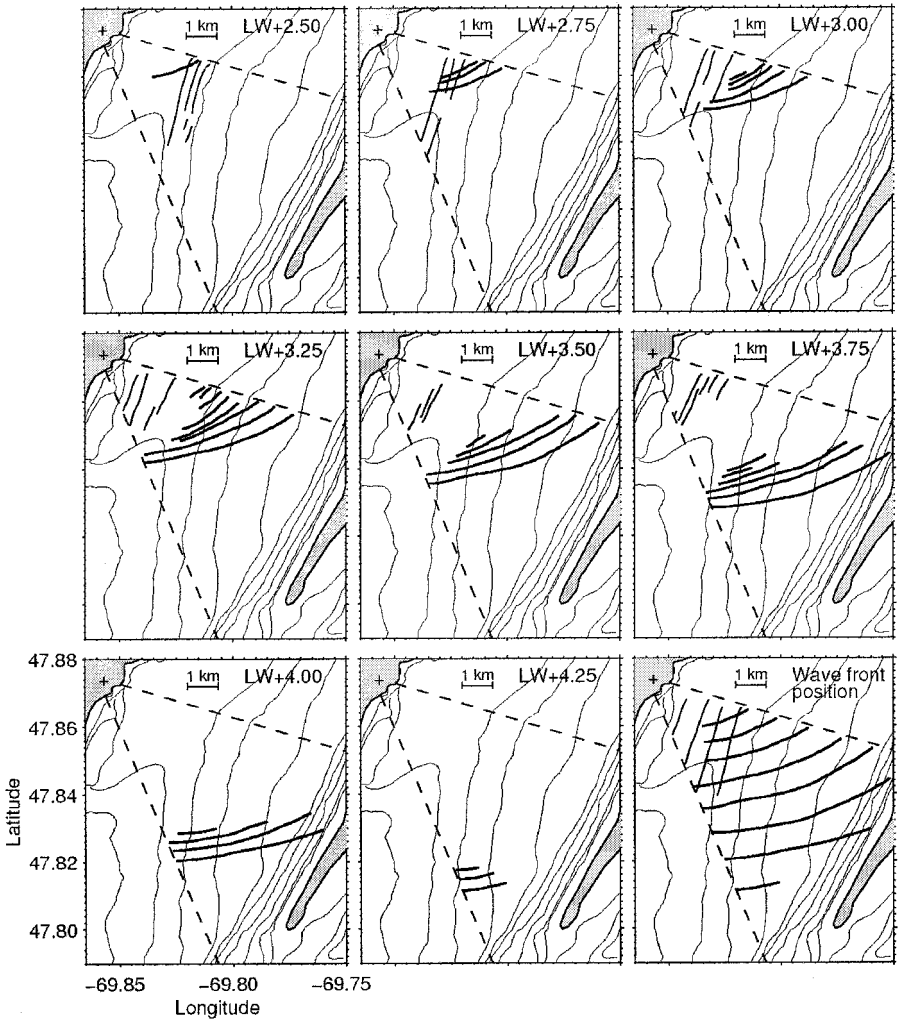


Figure 6. Position of wave features observed from Camera 1 on July 31, 2000. The dashed lines represent the angle of view of the camera. Wavetrains A and B are depicted by the thin and thick curves, respectively. The bottom right panel shows the wavetrains frontal positions at 15 min intervals.

with the LW + 3.00 panel on Fig. 6). This larger scale view shows the extent of the waves; the width of Wavetrain A is about 7 km while Wavetrain B appears to be as wide as the island is long (≈ 15 km). The aircraft view indicates that Wavetrain B collides almost perpendicularly, at the northeastern end of Ile-aux-Lièbres Island. This perpendicular wave incidence is in agreement with Camera 2.

Figure 8 also suggests that the wavetrains emanate from somewhere near the 120 m deep



Figure 7. Field of view (left panel) of Camera 2, looking northwest, showing surface manifestations of IWs (details on the right panel). These IWs propagate toward the camera. This image was taken on August 18, 2002, at LW + 2.75.

trough off Cap-de-la-Tête-aux-Chien (Fig. 1). Since the waves are observed early flood tide, it is plausible that they are generated as lee waves during the ebb tidal flow near the Cap-de-la-Tête-aux-Chien topographic depression. As the ebb flow relaxes, the lee waves may be released landward and may evolve into a series of solitary waves (Lee and Beardsley, 1974; Farmer and Smith, 1980; Lamb, 1994). Additional field observations would clarify this hypothesis.

4. Simulated internal solitary wave structure

Aspects of ISW propagation and structure can be examined with a two-dimensional model. We have set up such a model, with the appropriate hydrography for application to the North Channel. The model, described in Appendix A, has nonhydrostatic and fully nonlinear dynamics, so its simulations are less limited than the weakly nonlinear Korteweg-de-Vries (KdV) theory (Osborne and Burch, 1980), which we will also discuss in this section.

a. Model setup

The geometry of simulation was a rectangular basin 2500 m long and 70 m deep, with horizontal and vertical resolutions of $\Delta x = 5$ m and $\Delta z = 0.5$ m, respectively, and a time step of $\Delta t = 1$ s. These scales are appropriate for this domain, and the resolution is capable of handling the expected ISW scales. To generate an ISW, the isopycnals were initially depressed at the forcing end of the basin according to

$$a = 2a_0 \operatorname{sech}^2 [x/(2L)] \quad (1)$$

where a_0 varies from run to run and L is computed from the two-layer KdV theory via

$$a_0 L^2 = \frac{4}{3} \frac{(h_1 h_2)^2}{(h_2 - h_1)} \quad (2)$$

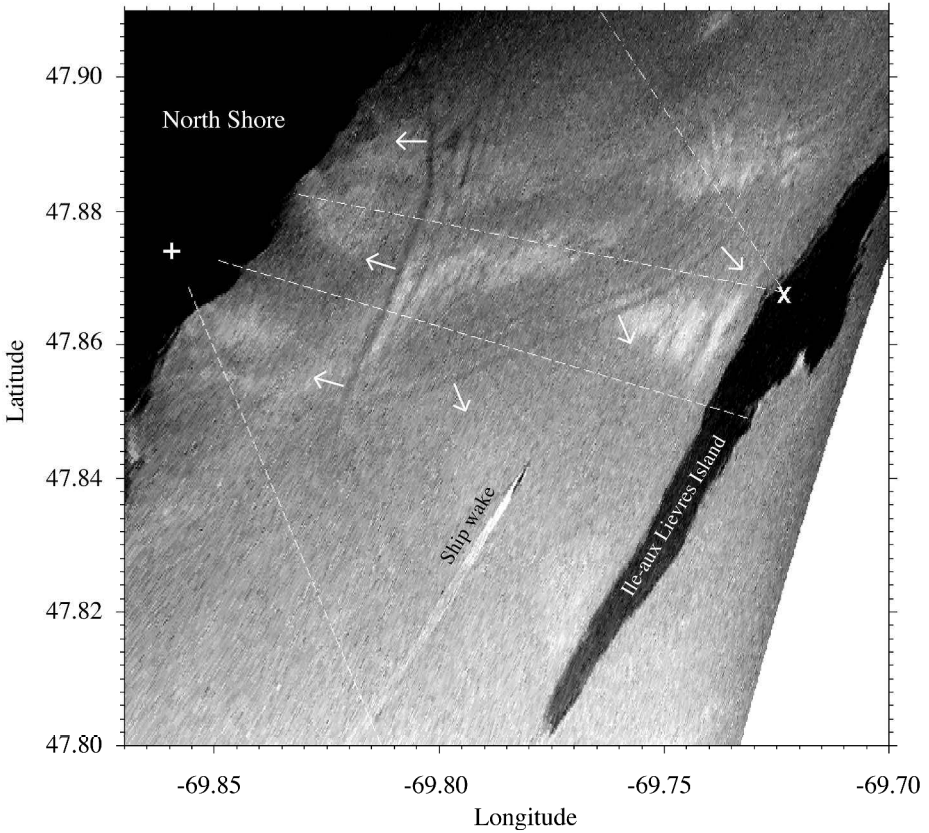


Figure 8. Aerial georectified photograph of banded surface patterns in the North Channel collected at LW + 3.00 on August 29, 2000. The arrows indicate the direction of propagation of the wavetrains. The dashed and dashed-dotted lines represent the field of view of Cameras 1 (plus) and 2 (cross).

(Bogucki and Garrett, 1993) where $h_1 = 9$ m and $h_2 = 61$ m are surface and bottom layer thicknesses, respectively. The initial velocity field is motionless. This initial condition mimics roughly the ISW generation method in the laboratory experiments of Michallet and Ivey (1999). We examined the wave solution once the leading ISW separates from smaller amplitude waves that also emerge from this initial condition.

A total of 26 simulations were made using three different background buoyancy frequency $N^2 = (g/\rho)\partial\rho/\partial z$, where g is gravity, ρ is density and z is the downward-pointing vertical axis (Fig. 3); 14 simulations were made using the observed profile, 6 using the least stratified and 6 using the most stratified conditions.

b. Wave structure

Figure 9 shows an example of an initial density field (left panel) used to generate a rightward propagating ISW (right panel). The ISW generated has an amplitude of 16 m, to

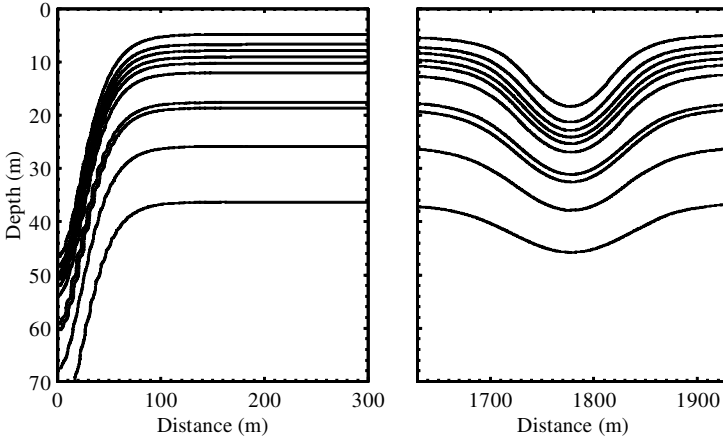


Figure 9. Example of an initial density field (left) used to generate a 16 m amplitude rightward propagating ISW (right). The contour interval is 0.5 kg m^{-3} .

match the leading ISW seen on the echogram (Fig. 2), and its phase speed is 0.78 m s^{-1} . This is consistent with the observed phase speed of Wavetrain B ($c_B = 0.8 \text{ m s}^{-1}$). Figure 10 shows the corresponding velocity field. The results for the horizontal component indicate a “shallow water” character of the wave, in that the whole water column is affected by its passage. For comparison with field measurements, the dashed-dotted lines on Figure 4 show the modeled magnitude of the horizontal and vertical velocities ($|U|$, $|W|$). The model results agree reasonably well with the observations. The discrepancies between the modeled and observed $|U|$ profile, especially noticeable in the depth intervals 0–15 m

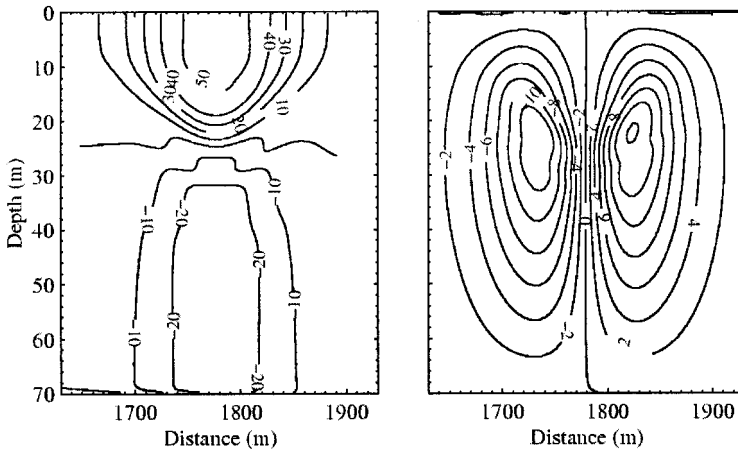


Figure 10. Horizontal (left panel) and vertical (right panel) velocity components corresponding to the ISW of Figure 9. The units are cm s^{-1} .

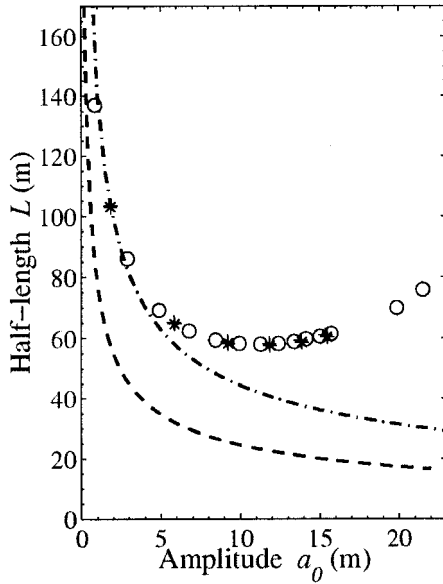


Figure 11. Relationship between wave half-length L and amplitude a_0 . The markers (circles, plus and stars) represent the solution from the nonhydrostatic model for the three background density stratifications examined. The dashed-dotted line is the continuously-stratified KdV solution and the dashed line is the two-layer KdV solution (Eq. 2) using $h_1 = 9$ m and $h_2 = 61$ m.

and 35–50 m, are attributed to other, nonwavy, baroclinic phenomena of unknown origins since there is no such equivalent in the $|W|$ profile.

The half-length of modeled ISWs was computed as

$$L = \frac{1}{2a_0} \int_{x_1}^{x_2} a \, dx \tag{3}$$

(Vlasenko *et al.*, 2000) where the interval between x_2 and x_1 includes the entire ISW but not the trailing high-frequency waves (e.g. the width of the right panel of Fig. 9). In continuously-stratified systems, amplitudes and wavelengths vary with depth (e.g., Vlasenko *et al.*, 2000). This depth dependence can be seen qualitatively on the right panel of Figure 9. For the following we only present the half-length and amplitude computed at the main pycnocline, located at 9 m depth, since this is the interface that can be identified on the echogram.

Figure 11 shows the relationship between L and a_0 as inferred from our model and compared with the two-layer theory (Eq. 2) and continuously-stratified KdV theory. For the continuously stratified case, an eigenfunction problem must be solved for the normal modes of oscillations (Sandstrom and Oakey, 1995). The continuous KdV theory agrees well with model results for $a_0 < 5$ m. It is worth noting that the two-layer theory

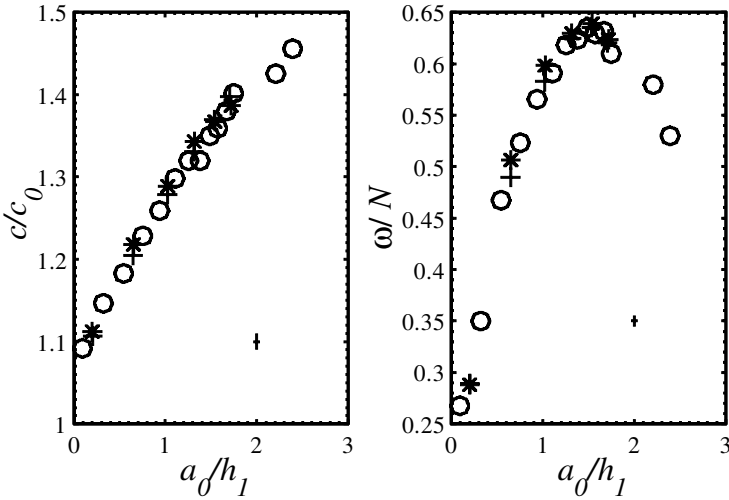


Figure 12. Dependency of wave phase speed c and frequency ω on amplitude a_0 . The axes are normalized by the linear internal phase speed c_0 , the buoyancy frequency N at the main pycnocline (i.e. 9 m) and the surface layer thickness h_1 , respectively. The markers (circles, plus and stars) represent the solutions from the three background density stratifications examined.

underestimates half-lengths by a factor of 2 or more. Note that for the two-layer case we could find another combination of layer thicknesses (h_1, h_2) that would give a better agreement but the natural choice, based on the echogram and density profiles, is to use the values we have picked ($h_1 = 9$ and $h_2 = 61$). For wave amplitudes greater than the surface layer thickness ($a_0 > 9$ m), the $L - a_0$ dependency reverses and half-length increases with amplitude, as opposed to the KdV theory (valid for $a_0 < h_1$), but in agreement with the fully nonlinear numerical simulations of Vlasenko *et al.* (2000).

According to Figure 11, a 16 m amplitude wave, such as the first wave seen on the echogram, has a half-length $L = 60$ m and a phase speed $c = 0.8 \text{ m s}^{-1}$. For comparison with the linear theory, Figure 12 shows ISWs phase speeds, normalized with the linear phase speed c_0 of long internal waves, as function of wave amplitudes. Over the range of parameters examined, the phase speed c increases almost linearly with the wave amplitude. The figure also shows the amplitude dependance of the wave angular frequency

$$\omega = \frac{\pi c}{L} \tag{4}$$

normalized with the buoyancy frequency N at the main pycnocline (9 m depth). The ISWs examined here are nonhydrostatic in nature since $\omega \sim N$ (Gill, 1982, p. 259). The figure also shows that the frequency of ISWs increases with wave amplitude up to a maximum $\omega_{\text{max}} \approx 0.65N$ after which it decreases.

c. Wave energy

The total energies (potential plus kinetic) of the modeled ISWs were computed by integrating over depth and between times t_1 and t_2 the energy flux through a vertical section (neglecting turbulent decay) (Gill, 1982, p. 76),

$$E_M = \int_0^H \int_{t_1}^{t_2} u \left[p' + \frac{1}{2} \rho (u^2 + w^2) \right] dt dz \quad (5)$$

where p' is the wave-induced pressure, ρ is density and u , w are horizontal and vertical velocities, respectively. The times t_1 and t_2 were chosen to include the entire ISW. For waves considered here, the nonlinear contribution in Eq. 5 represents up to 20% of total wave energy.

Assuming equipartition between potential and kinetic energy, valid for $a_0/h_1 \ll 1$, the total energy of an arbitrary shaped wave propagating in a two-layer system is (Bogucki and Garrett, 1993),

$$E = g \Delta \rho \int_{-\infty}^{\infty} a^2 dx \quad (6)$$

where g is gravity, $\Delta \rho$ is the density difference between bottom and top layers and $a(x)$ is the interface displacement. For an interfacial KdV wave having for solution $a = a_0 \operatorname{sech}^2(x/L)$ this yields

$$E_{\text{KdV}} = \frac{4}{3} g \Delta \rho a_0^2 L. \quad (7)$$

Figure 13 compares E_M and E_{KdV} . E_{KdV} was computed using our previous results for L and a_0 (Fig. 11) and values $\Delta \rho = (3.72, 4.96, 6.20) \text{ kg m}^{-3}$ for the three background stratifications examined. The tight correlation (slope $S = 0.85$; correlation coefficient squared $R^2 = 0.9998$; p -value < 0.001) between E_M and E_{KdV} shows that Eq. 7, and thus Eq. 6, are appropriate even for large-amplitude ($a_0 > h_1$) non-KdV waves in continuously stratified systems.

5. Results

The above analysis permits an indirect estimation of the vertical mixing resulting from wavetrain-boundary collisions. We focus on the simpler case of the perpendicular impact of Wavetrain B with the simple bathymetry of Ile-aux-Lièvres Island, leaving other collisions in the domain to future field investigations.

a. Wave structure

In order to use Eq. 6 to compute the total energy of the wavetrain seen on the echogram, it is necessary to convert the temporal dependence of isopycnal displacement $a(t)$ revealed

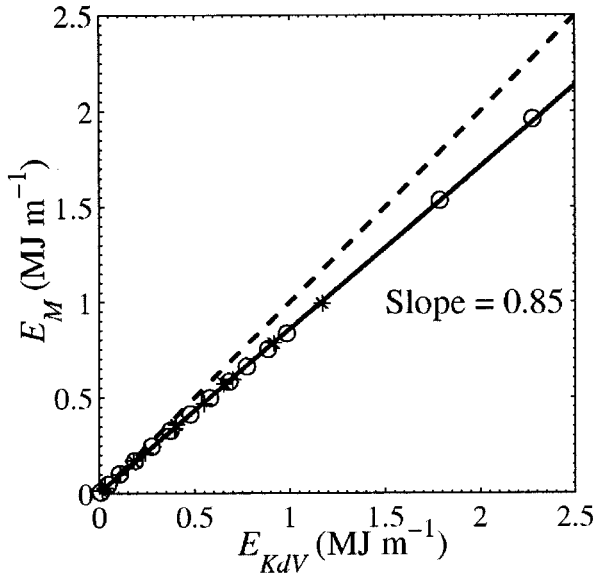


Figure 13. Relationship between wave energy as simulated by our nonhydrostatic model (E_M) and computed from Eq. 7 (E_{KdV}). The dashed line is the 1:1 line.

in the echogram to a spatial dependence $a(x)$ within the IW. This may be done by use of the $L - a_0$ relationship (Fig. 11). First, the function

$$a(t) = a_0 \operatorname{sech}^2 (t/T) \tag{8}$$

was fit to the observed interface of the leading ISW, where T is the apparent half-period (since the ship is moving) and t is time. The result is $a_0 = 16$ m and $T = 83$ s (see dashed line on Fig. 2). Figure 11 then yields a half-length of $L = 62$ m. Combining this with T yields a time-space conversion factor for the echogram (1 s on the echogram corresponds to 0.75 m).

Figure 14 shows the position of the echogram wave interface as function of space. The linear trend was removed to isolate the high-frequency waves from the lower frequency tendency. The total length of the wavetrain is thus calculated to be $\lambda \approx 10^3$ m, which is consistent with the length of the wavetrain B as estimated from shore-based imagery (Fig. 6).

b. Energetics

Using this wave interface displacement $a(x)$ in (6) with $\Delta\rho = 4.96 \text{ kg m}^{-3}$, $g = 9.81 \text{ m s}^{-2}$, and applying the correction factor $S = 0.85$, we obtain $\tilde{E} = 0.85E = 4.1 \text{ MJ m}^{-1}$ as the total wavetrain energy in mid-channel. This energy could be dissipated en route by several mechanisms.

According to the dissipation model of Sandstrom and Oakey (1995) an ISW loses energy

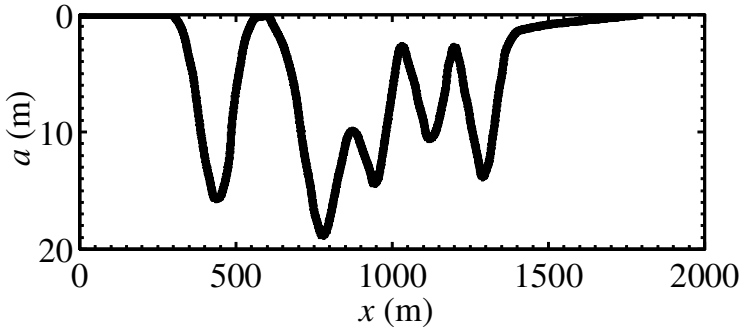


Figure 14. Vertical displacement of the interface of the wavetrain seen on Figure 2 as function of the inferred distance (see text). The linear trend was removed.

from wave-induced shear turbulence only if its amplitude a_0 exceeds a critical value given by

$$a_c = \left[\frac{c^2}{N^2 Ri_{\min}} \times \frac{1}{[1 + 2c^2/(N^2 L^2)]^2} \right]^{1/2} \quad (9)$$

where c is the phase speed and $Ri_{\min} = 1/4$ is the critical Richardson number below which shear instabilities will develop at the interface and enhance turbulent mixing. Using $N^2 = 4 \times 10^{-3} \text{ s}^{-2}$ (Fig. 3), $c = 0.8 \text{ m s}^{-1}$ and $L = 62 \text{ m}$, we calculate $a_c = 23 \text{ m}$. Since $a_0 < a_c$, we conclude that turbulent decay from wave-induced shear will cause negligible energy losses during IW transit across the channel.

Bottom friction will also extract energy from propagating IWs. Expressing the bottom shear stress in term of a drag coefficient (Gill, 1982, p. 328), the wave energy loss from bottom friction can be estimated as

$$\frac{\partial \tilde{E}}{\partial t} = -\rho_0 \int_0^\lambda C_d |u_2|^3 dx, \quad (10)$$

where C_d is a bottom drag coefficient and u_2 is the wave bottom layer velocity. Our simulations yield $u_2 = 0.22 \text{ m s}^{-1}$ for a 16 m amplitude ISW, with u_2 taken to be the average over the length $2L$ of the ISW. Using $\lambda = 10^3 \text{ m}$, a typical value for $C_d = 0.003$, and $\rho_0 = 1020 \text{ kg m}^{-3}$ we thus calculate $\partial \tilde{E}/\partial t = -33 \text{ W m}^{-1}$. At a phase speed of $c = 0.8 \text{ m s}^{-1}$ it takes $5 \times 10^3 \text{ s}$ to reach the base of the sloping boundary $4 \times 10^3 \text{ m}$, during which time the wavetrain is predicted to lose 0.16 MJ m^{-1} , roughly 4% of the total energy. The result is that the energy available for mixing at the base of the slope is $\tilde{E}_S = 3.9 \text{ MJ m}^{-1}$.

Upon IW collision with the sloping topography, some of the incident energy will be

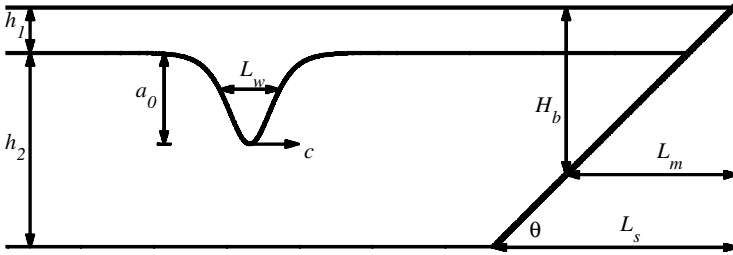


Figure 15. Schematic representation of a mode-1 ISW of amplitude a_0 and length L_w (equal to twice the half-length L) propagating in a two-layer system of depth h_1 and h_2 at a phase speed c . The wave heads toward the shoaling slope of length L_s and angle θ and will break at depth H_b , providing mixing over the internal surf zone of length L_m .

converted through mixing into increased potential energy, $\Delta\mathcal{P}$, of the water column. This has been represented as

$$\Delta\mathcal{P} = \gamma\tilde{E}_S. \tag{11}$$

by Michallet and Ivey (1999), in their laboratory study of ISWs colliding with linearly shoaling sidewalls, a geometry that is similar to the situation of the North Channel. The laboratory measurements suggest that γ depends on the ratio L_w/L_s where L_w is the length of an ISW, taking as twice its half-length L , and L_s is the length of the slope (Fig. 15).

The typical length of the sloping edge of Ile-aux-Lièvres Island is $L_s = 10^3$ m (Fig. 1). For the leading ISW on the echogram we have $L_w = 2L = 124$ m and thus $L_w/L_s = 0.124$. Examination of Figure 9 of Michallet and Ivey (1999) suggests the value $\gamma = 0.06$, i.e. that 6% of \tilde{E}_S goes into mixing, while their Figure 8 suggests that 15% of the incident energy is reflected back toward the source. Applying this value of γ to the observed wavetrain, we infer that the background potential energy will increase by $\Delta\mathcal{P} = 0.23 \text{ MJ m}^{-1}$ per wavetrain collision event.

c. Buoyancy flux and eddy diffusivity

Eq. 11 can be rewritten

$$\Delta\mathcal{P} = \int_0^\tau \int_0^{L_m} \int_0^H \overline{gw'\rho'} dz dx dt \tag{12}$$

where $\overline{gw'\rho'}$ is the vertical turbulent buoyancy flux (Osborn, 1980) from wave-induced boundary turbulence, L_m is the length of the internal surf zone (to be defined below) and τ is the period of the mixing event. This yields the depth-integrated buoyancy flux

$$J = \int_0^H \overline{gw'\rho'} dz = \frac{\Delta\mathcal{P}}{\tau L_m} \text{ [W m}^{-2}\text{]}. \tag{13}$$

To determine L_m , we note that the numerical simulations of Vlasenko and Hutter (2002) for slope collision of ISWs in continuously stratified environments, suggest that wave breaking occurs at a breaking depth H_b given by

$$\frac{a_0}{H_b - h_1} \cong \frac{0.8^\circ}{\theta} + 0.4 \quad (14)$$

where θ is the slope angle (Fig. 15). The shoaling slope along the northwestern edge of Ile-aux-Lièbres Island is $\theta = \tan^{-1}(40/1000) = 2.3^\circ$, varying little along the length of the island. Therefore, using $h_1 = 9$ m, we calculate $H_b = 30$ m for a 16 m amplitude ISW. We define the internal surf zone L_m to be the distance from the H_b isobath to the edge of the island, which yields $L_m = 700$ m in this instance.

An estimate for τ may be taken as the time it takes for a wave to travel back and forth from the breaking point to the island, that is $\tau = 2L_m/c$. With $c = 0.8$ m s⁻¹, this yields $\tau = 2 \times 10^3$ s as the mixing time.

The above values yield $J = 0.16$ W m⁻² as the buoyancy flux induced by the swashing of one wavetrain of the kind seen on the echogram over the length of the surf zone of Ile-aux-Lièbres Island. This may be expressed as an eddy diffusivity through (assuming $\overline{gw'\rho'} = \rho_0 K_p N^2$ (Osborn, 1980))

$$K_p = \frac{J}{\rho_0 N^2 H_p} \quad [\text{m s}^{-2}] \quad (15)$$

where ρ_0 is a reference density and H_p is the vertical scale within which mixing occurs. Using $\rho_0 = 1020$ kg m⁻³, $N^2 = 4 \times 10^{-3}$ s⁻² and $H_p = 15$ m (i.e. the thickness of the pycnocline in Fig. 3) we obtain $K_p = 3 \times 10^{-3}$ m² s⁻¹ for a single wavetrain per tidal cycle. In the case of n wavetrains per tidal cycle, this diffusivity would be increased by a factor of n .

6. Discussion: Shear- versus wave-induced mixing

Lacking direct measurements of mixing in the study region, we will infer background mixing rates, associated with the mean and tidal flows, from the three-dimensional, baroclinic numerical model of Saucier and Chassé (2000). This model resolves key aspects of the topography, e.g. the sloping bathymetry near Ile-aux-Lièbres Island, but the horizontal grid is too coarse (400 m) to resolve the IW field under discussion here. These authors produced maps (their Fig. 21) of the tidally-varying depth-integrated vertical turbulent buoyancy flux, parameterized following Mellor and Yamada (1974, 1982) and Kantha and Clayson (1994). Over a tidal cycle of average amplitude, the Saucier and Chassé model showed instantaneous hourly buoyancy fluxes of $J_{SC} < 0.002$ W m⁻² on the sloping flank of Ile-aux-Lièbres Island. During spring tide this number is increased by 1.5. This is 50 times less than our estimate, $J = 0.16$ W m⁻², of the buoyancy flux in the wave-swash zone, during a single wavetrain collision event.

It remains to determine whether these boundary mixing episodes are significant for the laterally- and tidally-averaged vertical diffusion in this stretch of the SLE. This may be done simply by replacing the length of the surf zone in (13) by the total width of the North Channel $L_m = 8 \times 10^3$ m, and the time of mixing by the semi-diurnal tidal period $\tau = 4 \times 10^4$ s. The calculation gives $\bar{J} = 6 \times 10^{-4} \text{ W m}^{-2}$ and $\bar{K}_p = 1 \times 10^{-5} \text{ m}^2 \text{ s}^{-1}$, where the overline indicates laterally and tidally averaging. By comparison, tidally- and laterally-averaged model values in the North Channel are $\bar{J}_{SC} < 4 \times 10^{-4} \text{ W m}^{-2}$ (left bottom panel on Fig. 21 from Saucier and Chassé). This suggests that mixing from IW breaking is not only dominant in narrow bands near boundaries, but may also account for a significant fraction of the laterally and tidally-averaged mixing.

7. Conclusions

This study of a portion of the partially mixed upper St. Lawrence Estuary reveals the presence of large-amplitude high-frequency internal waves forced by the tides. While the sites and mechanisms of IW generation are quite uncertain, remote sensing observations reveal their propagation patterns, and their collision with sloping boundaries. Our analysis indicates that the collision of a single wavetrain with one of the boundaries (Île-aux-Lièvres Island) can account for a significant fraction of the laterally- and tidally-averaged vertical diffusion. However, preliminary field observations (not shown here) suggest that there are two or more wavetrain-island collisions per tidal cycle. Additionally, mixing can be expected to occur on the other, unstudied, channel boundary. Taken together, these facts suggest that our estimate of net tidal mixing rates may represent a conservative lower bound.

These indirect inferences of wave-induced boundary mixing suggest that the process may be of general significance in partially-mixed estuaries. Testing this hypothesis would require *in situ* field observations of shear and/or scalar microstructure, as in Sandstrom and Oakey (1995), or measurements of Reynolds stresses from acoustic Doppler current profilers as in Lu *et al.* (2000). Such observations, combined with mean profiles of salinity, temperature and nutrient concentration, would clarify the role of IW boundary mixing in coastal systems, and thereby contribute to the goal of parameterization.

Acknowledgments. We would like to thank the reviewers for helpful comments as well as Rich Pawlowicz (University of British Columbia) for his advice on the use of time-lapse imaging of surface signatures of internal waves, and Greg Ivey (University of Western Australia) for general discussions about internal-wave mixing. We would also like to thank Charlie Walls (Dalhousie University) for helping us with image rectifications and Dr. François Saucier (Maurice-Lamontagne Institute) for providing one of the cameras. This work was funded by the Fonds de Recherche sur la Nature et les Technologies of Québec, the U.S. Office of Naval Research, the Natural Sciences and Engineering Research Council of Canada, and the Canadian Foundation for Climate and Atmospheric Sciences.

APPENDIX A

The model

The model used in this study is a nonhydrostatic extension of the free-surface model initially developed by Bourgault (2001) to study estuarine dynamics. The model solves the two-dimensional incompressible Navier-Stokes equations,

$$u_t + (u^2)_x + (uw)_z = -(1/\rho_0)p_x + (A_H u_x)_x + (A_V u_z)_z \quad (\text{A1})$$

$$w_t + (uw)_x + (w^2)_z = -(1/\rho_0)p_z + g + (A_H w_x)_x + (A_V w_z)_z \quad (\text{A2})$$

$$\rho_t + (u\rho)_x + (w\rho)_z = (K_H \rho_x)_x + (K_V \rho_z)_z \quad (\text{A3})$$

$$u_x + w_z = 0 \quad (\text{A4})$$

where t is the time, x is the horizontal coordinate, z is the vertical coordinate with its origin at the undisturbed sea surface and positive downward, the subscripts t , x and z represent partial derivatives with respect to this variable, u is the horizontal velocity, w is the vertical velocity, p is the pressure, ρ_0 is a constant reference density, ρ is the density, g is gravity and A_H , A_V , K_H and K_V are coefficients of eddy viscosity and diffusivity.

Variables are arranged on a C -grid (Arakawa, 1966). Time derivative is discretized using a two-time level semi-implicit Crank-Nicholson numerical scheme and all spatial derivatives are centered. The equations are split relative to each spatial directions. This reduces the two-dimensional implicit problem into a sequence one dimensional implicit problem involving the inversion of tridiagonal matrix. The inversions are accomplished using a compact LU decomposition (Press *et al.*, 1992). The position of the free surface is computed semi-implicitly following Wang and Kravitz (1980). The nonhydrostatic algorithm uses a fractional step formulation following Jankowski (1999) and the resulting Poisson equation for the pressure is solved using a preconditioned conjugate gradient method as in Marshall *et al.* (1997).

Horizontal turbulent diffusion is parameterized following Smagorinsky (1963)

$$A_H = (C_S \Delta x)^2 |u_x| + A_0, \quad K_H = (C_S \Delta x)^2 |u_x| + K_0 \quad (\text{A5})$$

where C_S is the Smagorinsky coefficient, Δx is the horizontal grid size and A_0 and K_0 are constant background values. Values used for the simulations presented in this paper are $C_S = 0.7$, $A_0 = K_0 = 10^{-3} \text{ m}^2 \text{ s}^{-1}$. Coefficients of vertical turbulent diffusion are set to $A_V = 10^{-4} \text{ m}^2 \text{ s}^{-1}$, $K_V = 10^{-5} \text{ m}^2 \text{ s}^{-1}$.

REFERENCES

- Alford, M. H. 2003. Redistribution of energy available for ocean mixing by long-range propagation of internal waves. *Nature*, **423**, 159–162.
- Arakawa, A. 1966. Computational design for long-term numerical integration of the equations of fluid motion: Two-dimensional incompressible flow. *Part I. J. Comput. Phys.*, **1**, 119–143.
- Armi, L. 1978. Some evidence for boundary mixing in the deep ocean. *J. Geophys. Res.*, **83**, 1971–1979.

- Bogucki, D. and C. Garrett. 1993. A simple model for shear-induced decay of an internal solitary wave. *J. Phys. Oceanogr.*, *23*, 1767–1776.
- Bourgault, D. 2001. Circulation and mixing in the St. Lawrence Estuary, Ph.D. thesis, McGill University, Montreal, Quebec, Canada, 127 pp.
- Bourgault, D. and V. G. Koutitonsky. 1999. Real-time monitoring of the freshwater discharge at the head of the St. Lawrence Estuary. *Atmos. Ocean*, *37*, 203–220.
- Bourgault, D., F. J. Saucier and C. A. Lin. 2001. Shear instability in the St. Lawrence Estuary, Canada: A comparison of fine-scale observations and estuarine circulation model results. *J. Geophys. Res.*, *106*, 9393–9409.
- DeGuise, J. C. 1977. High frequency internal waves in the St. Lawrence Estuary, Master's thesis, McGill University, Montreal, Quebec, Canada.
- Dickie, L. and L. M. Trites. 1983. The Gulf of St. Lawrence, *in* *Estuaries and Enclosed Seas*, B. H. Ketchum, ed., Elsevier, 403–425.
- Dyer, K. R. 1988. Tidally generated estuarine mixing processes, *in* *Hydrodynamics of Estuaries, 1, Estuarine Physics*, B. Kjerfve, ed., CRC Press, Boca Raton, FL, 41–57.
- El-Sabh, M. 1988. Physical oceanography of the St. Lawrence Estuary, *in* *Hydrodynamics of Estuaries, 2, Estuarine Case Studies*, B. Kjerfve, ed., CRC Press, Boca Raton, FL, 61–78.
- Farmer, D. M. and H. Freeland. 1983. The physical oceanography of fjords. *Progr. Oceanogr.*, *12*, 147–220.
- Farmer, D. M. and J. D. Smith. 1980. Tidal interaction of stratified flow with a sill in Knight Inlet. *Deep-Sea Res.*, *27A*, 239–254.
- Forrester, W. D. 1974. Internal tides in St. Lawrence Estuary. *J. Mar. Res.*, *32*, 55–66.
- Galbraith, P. S. 1992. Relating overturns to mixing and buoyancy flux, Ph.D. thesis, Dalhousie University, Halifax, Nova Scotia, Canada, 243 pp.
- Galbraith, P. S. and D. E. Kelley. 1996. Identifying overturns in CTD profiles. *J. Atmos. Oceanic Technol.*, *13*, 688–702.
- Garrett, C., P. MacCready and P. Rhines. 1993. Boundary mixing and arrested Ekman layers: Rotating stratified flow near a sloping boundary. *Ann. Rev. Fluid Mech.*, *25*, 291–323.
- Geyer, W. R. 1993. The importance of suppression of turbulence by stratification on the estuarine turbidity maximum. *Estuaries*, *16*, 113–125.
- Geyer, W. R. and J. D. Smith. 1987. Shear instability in a highly stratified estuary. *J. Phys. Oceanogr.*, *17*, 1668–1679.
- Gill, A. E. 1982. *Atmosphere-Ocean Dynamics*, Academic Press, San Diego, CA, 662 pp.
- Goudsmit, G. H., F. Peeters, M. Gloor and A. Wuest. 1997. Boundary versus internal mixing in stratified natural waters. *J. Geophys. Res.*, *102*, 27,903–27,914.
- Government of Canada. 1997. Atlas of tidal currents from Cap de Bon-Désir to Trois-Rivières, Canadian Hydrographic Service, Fisheries and Oceans Canada, Ottawa.
- 2000. Canadian tide and currents tables, Vol. 3: St. Lawrence and Saguenay rivers, Canadian Hydrographic Service, Fisheries and Oceans Canada, Ottawa.
- Holland, K. T., R. A. Holman, T. C. Lippmann, J. Stanley and N. Plant. 1997. Practical use of video imagery in nearshore oceanographic field studies. *IEEE J. Oceanic Eng.*, *22*, 81–91.
- Imberger, J. and P. Hamblin. 1982. Dynamics of lakes, reservoirs and cooling ponds. *Ann. Rev. Fluid Mech.*, *14*, 153–187.
- Imberger, J. and G. N. Ivey. 1991. On the nature of turbulence in a stratified fluid. Part II: Application to lakes. *J. Phys. Oceanogr.*, *21*, 659–680.
- Ingram, R. G. 1978. Internal wave observation off Isle Verte. *J. Mar. Res.*, *36*, 715–724.
- Jankowski, J. A. 1999. A non-hydrostatic model for free surfaces flows, Ph.D. thesis, University of Hannover, Germany, 251 pp.

- Jay, D. A. and J. D. Smith. 1990a. Residual circulation in shallow estuaries 1. Highly stratified, narrow estuaries. *J. Geophys. Res.*, *95*, 711–731.
- 1990b. Residual circulation in shallow estuaries 2. Weakly stratified and partially mixed, narrow estuaries. *J. Geophys. Res.*, *95*, 733–748.
- Kantha, L. H. and C. A. Clayson. 1994. An improved mixed layer model for geophysical applications. *J. Geophys. Res.*, *99*, 25,235–25,266.
- Kay, D. J. and D. A. Jay. 2003a. Interfacial mixing in a highly stratified estuary. 1. Characteristics of mixing. *J. Geophys. Res.*, *108*, 3072.
- 2003b. Interfacial mixing in a highly stratified estuary. 2. A “method of constrained differences” approach for the determination of the momentum and mass balances and the energy of mixing. *J. Geophys. Res.*, *108*, 3073.
- Koutitonsky, V. G. and G. L. Bugden. 1991. The physical oceanography of the Gulf of St. Lawrence: A review with emphasis on the synoptic variability of the motion, *in* The Gulf of St. Lawrence: Small Ocean or Big Estuary? J. C. Theriault, ed., *Can. Spec. Publ., Fish. Aquat. Sci.*, *113*, 57–90.
- Lamb, K. G. 1994. Numerical experiments of internal wave generation by strong tidal flow across a finite amplitude bank edge. *J. Geophys. Res.*, *99*, 843–864.
- Lee, C.-Y. and R. C. Beardsley. 1974. The generation of long nonlinear internal waves in a weakly stratified shear flow. *J. Geophys. Res.*, *79*, 453–462.
- Legendre, L. 1981. Hydrodynamic control of marine phytoplankton production: The paradox of stability, *in* Echohydrodynamics, J. C. J. Nihoul, ed., Elsevier, Amsterdam, 191–207.
- Lu, Y., R. G. Lueck and D. Huang. 2000. Turbulence characteristics in a tidal channel. *J. Phys. Oceanogr.*, *30*, 855–867.
- MacIntyre, S., K. M. Flynn, R. Jellison and J. Romero. 1999. Boundary mixing and nutrient fluxes in Mone Lake, California. *Limnol. Oceanogr.*, *44*, 512–529.
- Marshall, J., A. Adcroft, C. Hill, L. Perelman and C. Heisey. 1997. A finite-volume, incompressible Navier Stokes model for studies of the ocean on parallel computers. *J. Geophys. Res.*, *102*, 5753–5766.
- Mellor, G. L. and T. Yamada. 1974. A hierarchy of turbulence closure models for planetary boundary layers. *J. Atmos. Sci.*, *31*, 1791–1806.
- 1982. Development of a turbulence closure model for geophysical fluid problems. *Rev. Geophys. Space Phys.*, *20*, 851–875.
- Mertz, G. and Y. Gratton. 1990. Topographic waves and topographically induced motion in the St. Lawrence Estuary, *in* Oceanography of a Large-Scale Estuarine System: The St. Lawrence, M. I. El-Sabh and N. Silverberg, eds., Springer-Verlag, NY, 94–108.
- Michallet, H. and G. N. Ivey. 1999. Experiments on mixing due to internal solitary waves breaking on uniform slopes. *J. Geophys. Res.*, *104*, 13,467–13,477.
- Muir, L. R. 1979. Internal tides in the middle estuary of the St. Lawrence. *Naturaliste Can.*, *106*, 27–36.
- 1981. Variability of temperature, salinity and tidally-averaged density in the middle estuary of the St. Lawrence. *Atmos. Ocean*, *4*, 320–336.
- Munk, W. H. 1966. Abyssal recipes. *Deep-Sea Res.*, *13*, 707–730.
- Munk, W. H. and C. Wunsch. 1998. Abyssal recipes II: Energetics of tidal and wind mixing. *Deep-Sea Res. I*, *45*, 1977–2010.
- Osborn, T. R. 1980. Estimates of the local rate of vertical diffusion from dissipation measurements. *J. Phys. Oceanogr.*, *10*, 83–89.
- Osborne, A. R. and T. L. Burch. 1980. Internal solitons in the Andaman Sea. *Science*, *208*, 451–459.
- Pawlowicz, R. 2003. Quantitative visualization of geophysical flows using low-cost oblique digital time-lapse imaging. *IEEE J. Oceanic. Eng.*, *28*, (in press).
- Perkin, R. G. and E. L. Lewis. 1978. Mixing in an Arctic fjord. *J. Phys. Oceanogr.*, *8*, 873–880.

- Peters, H. and R. Bokhorst. 2000. Microstructure observations of turbulent mixing in a partially mixed estuary. Part I: Dissipation rates. *J. Phys. Oceanogr.*, *30*, 1232–1244.
- Press, W., S. Teukolsky, W. Vetterling and B. Flannery. 1992. Numerical recipes in FORTRAN, 2nd edition, Cambridge University Press, 992 pp.
- Reid, S. J. 1977. Circulation and mixing in the St. Lawrence Estuary near Ilet Rouge. Bedford Inst. Oceanogr. Tech. Report Series/BI-R-77.
- Sandstrom, H. and N. S. Oakey. 1995. Dissipation in internal tides and solitary waves. *J. Phys. Oceanogr.*, *25*, 604–614.
- Saucier, F. J. and J. Chassé. 2000. Tidal circulation and buoyancy effects in the St. Lawrence Estuary. *Atmos. Ocean*, *38*, 1–52.
- Simard, Y. 1985. Exploitation de l'acoustique sous-marine pour l'étude de la répartition spatiale et des rythmes de broutage du plancton dans un environnement turbulent. Ph.D. thesis, Université Laval, Québec, Québec.
- Smagorinsky, J. 1963. General circulation experiments with primitive equations. I. The basic experiment. *Mon. Weather Rev.*, *91*, 99–164.
- Stacey, M. T., S. G. Monismith and J. Bureau. 1999. Observations of turbulence in a partially stratified estuary. *J. Phys. Oceanogr.*, *29*, 1950–1970.
- Stigebrandt, A. 1976. Vertical diffusion driven by internal waves in a sill fjord. *J. Phys. Oceanogr.*, *6*, 486–495.
- 1979. Observational evidence for vertical diffusion driven by internal waves of tidal origin in the Oslo fjord. *J. Phys. Oceanogr.*, *9*, 435–441.
- Stigebrandt, A. and J. Aure. 1989. Vertical mixing in basin waters of fjords. *J. Phys. Oceanogr.*, *19*, 917–926.
- Vlasenko, V., P. Brandt and A. Rubino. 2000. Structure of large-amplitude internal solitary waves. *J. Phys. Oceanogr.*, *30*, 2172–2185.
- Vlasenko, V. and K. Hutter. 2002. Numerical experiments on the breaking of solitary internal waves over a slope-shelf topography. *J. Phys. Oceanogr.*, *32*, 1779–1793.
- Wang, D.-P. and D. W. Kravitz. 1980. A semi-implicit two-dimensional model of estuarine circulation. *J. Phys. Oceanogr.*, *10*, 441–454.

Received: 1 April, 2003; revised: 28 July, 2003.